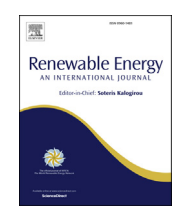


Contents lists available at ScienceDirect

Renewable Energy

journal homepage: www.elsevier.com/locate/renene



Activated alumina as value-added byproduct from the hydrolysis of hierarchical nanoporous aluminum with pure water to generate hydrogen fuel



Timothy Lee ^a, Jintao Fu ^a, Victoria Basile ^b, John S. Corsi ^{a, c}, Zeyu Wang ^{a, d}, Eric Detsi ^{a, c, *}

- ^a Department of Materials Science & Engineering, University of Pennsylvania, Philadelphia, PA, 19104-6272, USA
- ^b Department of Chemistry & Biochemistry, University of California Los Angeles, Los Angeles, CA, 90095-1569, USA
- ^c Vagelos Institute for Energy Science and Technology (VIEST), Philadelphia, PA, 19104, USA
- ^d State Key Laboratory of Advanced Welding and Joining, Harbin Institute of Technology, Harbin, 150001, China

ARTICLE INFO

Article history: Received 24 July 2019 Received in revised form 2 March 2020 Accepted 12 March 2020 Available online 17 March 2020

Keywords:
Nanoporous aluminum
Metal hydrolysis
Bayerite aluminum hydroxide
High surface area activated alumina
Eta-alumina

ABSTRACT

The sale of value-added byproducts from hydrogen-generating reactions is a strategic approach to lower the costs of hydrogen fuel in order to realize a truly sustainable hydrogen economy. Metal hydrolysis is a chemical process that produces hydrogen together with a metal hydroxide species; however, this reaction is rarely observed without chemical additives or extreme reaction conditions. Previously, we demonstrated that hierarchical nanoporous aluminum can create hydrogen at standard conditions for temperature and pressure via hydrolysis without any additives. The advantage of this method is the coproduction of pure aluminum hydroxide (Al(OH)₃). Here we explore the transformation of this Al(OH)₃ hydrolysis byproduct into valuable materials to elucidate strategies in reducing the overall cost of hydrogen generated. In particular, we demonstrate in this work that (i) the synthesis of hierarchical nanoporous aluminum is scalable to meet the needs of large-scale production for a hydrogen economy, and (ii) the Al(OH)₃ hydrolysis byproduct can be transformed to create high surface-area "activated alumina" (Al₂O₃) as a commercially viable product.

© 2020 Elsevier Ltd. All rights reserved.

1. Introduction

The absence of scalable and sustainable hydrogen (H₂) production methods prevents widescale adoption of a H₂ economy. Current H₂ production methods are not sustainable; over 95% of H₂ used worldwide is produced through steam reforming of natural gas, which heavily depends on fossil fuels. Additionally, undesirable carbon dioxide (CO₂) is co-produced during the process [1]. Water splitting by electrolysis, thermolysis, and photoelectrolysis represent promising sustainable methods to produce H₂ [2,3]. However, the costs of these processes are much higher than that of steam reforming as illustrated in Table 1, adapted from reference. [3].

Co-production of sustainable H₂ with value-added products represents an alternative approach to reduce the cost of H₂ through

E-mail address: detsi@seas.upenn.edu (E. Detsi).

the sale of these byproducts. For example, co-producing H_2 and graphitic carbon without CO_2 emissions by heat-induced decomposition of methane (CH₄) over metallic catalysts through Eq. (1), has been widely investigated as an alternative route to sustainable H_2 [4–7]:

$$CH_4\left(g\right) \rightarrow 2H_2\left(g\right) + C(s)\left(\Delta H^\circ = 74 \text{ kJ/mol}\right) \tag{1}$$

However, the catalytic activity of metallic nanoparticles (Ni, Fe, and Co) used to promote the thermocatalytic decomposition of CH_4 into H_2 and carbon decreases over time due to the heat-induced coarsening and clustering of these nanoparticles, the deposition of carbon on the nanoparticles, and the structural changes caused by carbon diffusion in the nanoparticles [5–11]. These three issues result in loss of catalytic activity, which represents the main challenge in the field [5,6,12–14]. Recently in ACS Sustainable Chemistry & Engineering [15], we reported on the co-production of H_2 , aluminum hydroxide (Al(OH)3), and heat by hydrolysis of novel hierarchical nanoporous aluminum (NP–Al) in pure water (i.e. water without any additives to catalyze the hydrolysis reaction)

^{*} Corresponding author. Department of Materials Science & Engineering, University of Pennsylvania, Philadelphia, PA, 19104-6272, USA.

Table 1Common H₂ production processes. ^(a)Rate based on 30 tons of H₂/day, and assuming the sale of reaction by-products.

Process	Overall efficiency [%]	Capital cost [M\$]	Hydrogen cost [\$/kg]	Reaction byproducts
Steam reforming	74-85%	226.4	+2.27	CO ₂ (undesirable)
Electrolysis	40-60%	504.8-499.6	+5.89 - 6.03	O ₂ (useless)
Thermolysis	20-45	39.6-2107.6	+2.17 - 2.63	O ₂ (useless)
		5.7-16	+7.98 - 8.40	
Photo-electrolysis	0.06	Not available	+10.36	O ₂ (useless)
Hydrolysis of nanoporous aluminum in pure water	36–38%	~156.1ª	-2.63 ^a	Al ₂ O ₃ (useful) Heat (useful)

through the reaction in Eq. (2) [15]:

$$2Al(s) + 6H_2O(1) \rightarrow 2Al(OH)_3(s) + 3H_2(g) + heat$$
 (2)

The high carbon footprint associated with the production of primary aluminum is an issue for the sustainability of this process [16,17]. Therefore, for the source of aluminum in Eq. 2, (i) we propose to use carbon-free primary aluminum from Elysis in the long term [17], when it is commercially available [17]. (ii) In the short term, secondary aluminum (i.e. recycled aluminum) can be used to minimize the carbon footprint of H₂. Indeed, the global market of recycled aluminum was over 22 million tons in 2016 with projections to reach over 29 million tons in 2026 [18]. Assuming an H₂ production rate of 30 tons per day, which corresponds to 10,950 tons of H₂ per year (US Department of Energy target: 1-100 tons/day [19]), the amount of recycled aluminum needed for this purpose will be 98,550 tons per year, which only represents 0.34% of the 2026 secondary aluminum forecast. Therefore, sustainable H₂ production through the reaction in Eq. (2) using secondary aluminum has the potential to contribute to the global H₂ need, provided that the process is scalable and costeffective.

To create a scalable and cost-effective process, the usefulness of the byproducts generated in Eq. (2) must be evaluated. The solid byproduct, Al(OH)3, can either be recycled back into metal Al (for example through the Elysis carbon-free Al smelting process [17]), or be transformed into another valuable product. Here we explore the latter as a cost-effective measure to justify scalability of this hydrogen-generating method. In our previous work [15], we focused on the processing of hierarchical nanoporous aluminum and its unique ability to generate hydrogen through Eq. (2) at standard temperature and pressure and without any chemical additives. The present work is aimed at (i) demonstrating the scalability of our synthesis process for large-scale production of hierarchical nanoporous aluminum and (ii) the production of activated alumina (Al_2O_3) with high specific surface area, from the $Al(OH)_3$ co-produced with H_2 through Eq. (2). The term "activated alumina" refers to the thermal decomposition product of Al(OH)₃ in which heating causes an "activation" or change in its surface structure and elemental composition to create a high specific surface area. As a result, this material exhibits high surface area, high thermal stability, and surface acidity and interaction with deposited transitional metals [20-22]. Thanks to these unique properties, activated alumina is widely used in several applications including inert high surface area catalyst support, water filtration for fluoride treatment, hydrocarbon impurity capture in the automobile and petroleum industries, and as a desiccant for drying gases [23–25]. Alumina has several metastable transition phases $(\gamma -, \eta -, \chi -, \delta -, \theta -, \kappa -, \text{ and } \alpha - \text{Al}_2\text{O}_3)$ with the low temperature phases $(\gamma_{-}, \eta_{-}, \text{ and } \gamma_{-}\text{Al}_{2}\text{O}_{3})$ having the most important and valuable industrial applications [26,27]. Thus, analysis of the Al byproduct formed can elucidate measures to create valuable industrial materials and reduce the overall cost of hydrogen production through the hydrolysis reaction in Eq. (2).

2. Experimental methods

2.1. Scaling up the synthesis of nanoporous aluminum

Hierarchical nanoporous aluminum (NP–AI) is made by air-free selective electrolytic removal of magnesium (Mg) from Mg-rich Al–Mg parent alloys with a typical composition of Al₃₀Mg₇₀ at. %. In this cell configuration, the Al₃₀Mg₇₀ parent alloy is used as the working electrode, pure Mg foil used as the counter and reference electrodes, and 0.4 M all-phenyl complex (APC) used as the electrolyte. The procedure for developing the APC electrolyte can be found in our earlier publications [28,29]. During selective electrolytic leaching, Mg is stripped from the Al–Mg working electrode and plated onto the Mg foil counter electrode, which makes it possible to recover Mg as demonstrated previously [15]. Recovered Mg can be used to make new Al–Mg parent alloys, which is necessary for the sustainability and affordability of the process.

In our previous work, we reported on this new air-free electrolytic dealloying concept using a monolithic bulk Al-Mg parent alloy with a few millimeters thickness [15]. Mg removal from such a thick sample took several weeks since the process is diffusioncontrolled. This long dealloying time is obviously undesirable for the scalability of the process. Therefore, in addition to investigating the conversion of Al(OH)₃ byproduct into activated Al₂O₃ with high specific surface area, the present work is also aimed at demonstrating the scalability of our process. In doing so, we modify our original synthesis procedure to obtain a twenty-fold increase in production capabilities. Specifically, the following three key modifications of our original synthesis procedure are performed for larger and faster batches: (i) the ionic conductivity of the APC electrolyte was further improved by introducing 0.4 M of lithium chloride (LiCl powder, >99.98%, Sigma Aldrich) [30]. (ii) Instead of using a monolithic thick Al₃₀Mg₇₀ parent alloy as the working electrode, we used small-sized, crushed pieces (thus in the powder form) of the same Al₃₀Mg₇₀ composition in a mesh pouch to expose more surface area to the electrolyte during Mg removal. In a typical process, the Al₃₀Mg₇₀ parent alloy was created by melting pure Al (shots, Alfa Aesar, 99.9%) and pure Mg (chips, Sigma Aldrich, 99.98%) at 900 °C in a graphite crucible using a tube furnace (OTF-1200X, MTI Corporation) with a quartz tube under argon gas flow. Next, the parent alloy (which is brittle in nature due to the presence of the Al₁₂Mg₁₇ intermetallic phase in Mg-rich Al–Mg alloys) was ground using a mortar and pestle in an argon-filled glove box into finer pieces near 1 mm in width. These pieces were loaded into a working electrode pouch made of stainless steel #120 mesh (0.125 mm openings). (iii) Instead of a single working and counter electrode, multiple alternating working and counter electrodes were used in parallel as shown in Fig. 1a and b. While for the present work we demonstrate the use of two Al₃₀Mg₇₀ working electrodes (red arrows Fig. 1b) alternating with three Mg foils counter electrodes (blue arrows Fig. 1b), this configuration can be

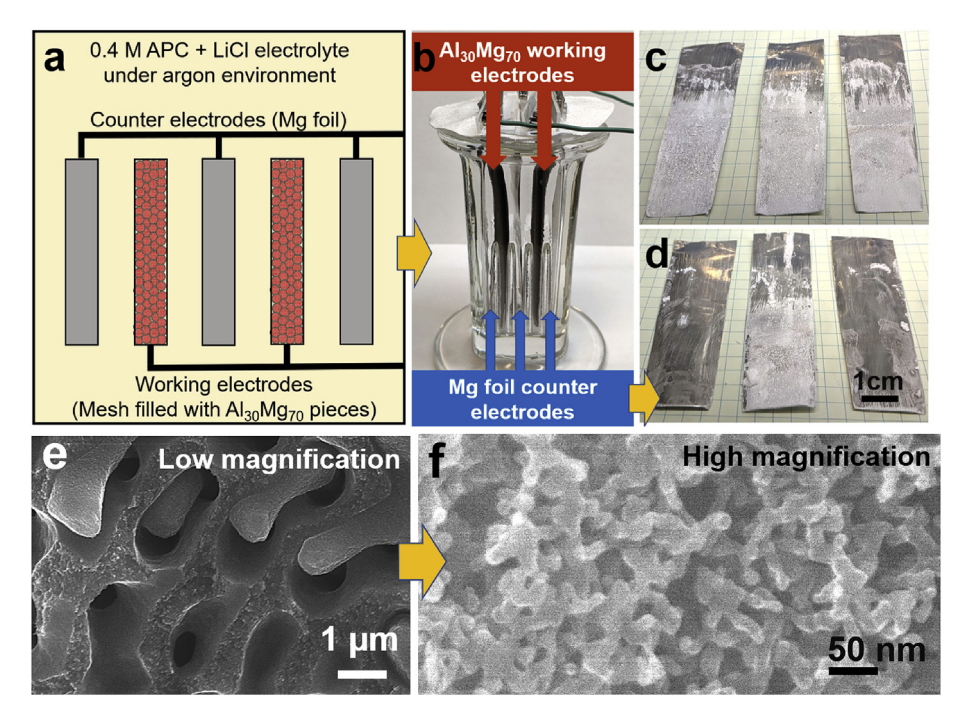


Fig. 1. (a) Schematic of a large-scale dealloying chamber electrode layout. (b) Dealloying chamber before addition of electrolyte. Crushed Al₃₀Mg₇₀ particles are loaded into a stainless steel mesh and used as the working electrode (red arrows); alternating Mg foils (blue arrows) serve as the counter electrodes. (**c**–**d**) Front and back sides of the three Mg foil counter electrodes after dealloying. Mg is plated on both sides of the middle electrode. (**e**) Low and (**f**) high magnifications SEM images of the hierarchical nanoporous aluminum morphology formed at the working electrodes. (For interpretation of the references to color in this figure legend, the reader is referred to the Web version of this article.)

further scaled up for larger applications by increasing the number of alternating electrodes. The selective electrolytic removal of Mg was carried out using a Bio-Logic VMP-300 potentiostat inside a MBRAUN argon-filled glove box with $\rm H_2O$ and $\rm O_2$ levels under 0.1 ppm. A constant potential of 0.45 V vs Mg/Mg $^{2+}$ was applied. The Mg dissolution current is measured between the working and counter electrodes and monitored for completion in which NP-Al is collected and rinsed with THF for the next step.

2.2. Gas chromatography study of H_2 production by hydrolysis of nanoporous aluminum with pure water

Gas chromatography (GC) was used to quantitatively study the hydrogen production rate by hydrolysis. NP-Al was sealed in a three-neck round bottom flask using a rubber septum under an argon atmosphere to prevent oxidation. Deionized (DI) $\rm H_2O$ was then sparged with nitrogen gas for 10 min before injection via a syringe into the reaction flask. Helium carrier gas (99.9999% purity, Airgas) was flowed through the flask to push the gas product into GC. A Pulsed Discharge Detector (PDD) with a Molecular Sieve 5A packed column was used to quantitatively determine the amount of hydrogen produced over time.

2.3. Co-production of H_2 , $Al(OH)_3$, and heat by hydrolysis of nanoporous aluminum with pure water

The synthesized hierarchical NP-Al pieces were further ground (note that dealloyed nanoporous metals are brittle) from mm-sized pieces into a fine powder in the argon glove box using a mortar and pestle. The powder was brought into a round bottom flask together with a stir bar and sealed using a rubber septum before removal from the argon glove box. DI H₂O was flushed with argon gas for 10 min to remove dissolved oxygen from this water and then injected in excess into the round bottom flask with NP-Al. The ratio of water to aluminum used was 3 mL of H₂O per 100 mg of NP-Al for

a large molar excess of H₂O. Injection of water resulted in rapid formation of hydrogen gas, which increased the pressure in the sealed system. This pressure was relieved as necessary via syringe. The flask was stirred for the desired length of time. Color change of the powder from black to white was observed after 3-4 days, indicating that most of the NP-Al has been converted into Al(OH)₃. Bubbles from hydrogen gas formation in the flask were no longer visibly observed after 6 days. After bubbling stopped, Al(OH)₃ was removed by centrifugation, rinsed with acetone, and then dried under vacuum overnight before further use in experiments. In the present work, the products studied are formed after reacting NP-Al with H₂O for 7 days; this represents a complete transformation as no more bubble formation is observed. Incomplete transformation where the products were analyzed before the color change from black to white after only three days is included in the supplementary information.

2.4. Dehydroxylation of $Al(OH)_3$ into activated alumina with high specific surface area

General dehydroxylation of Al(OH)₃ is based on similar procedures in the literature to remove hydroxide groups (-OH) from Al(OH)₃ in the form of water. These procedures have been shown to create high surface area Al₂O₃ nanostructures described as "activated alumina" for catalytic purposes [26,31,32]. In this research, Al(OH)₃ was heated to 600 °C for 12 h in an alumina crucible using a MTI Tube Furnace and an open quartz tube exposed to air. The Al₂O₃ product was then used as is for further characterization.

2.5. Materials characterization

A customized gas chromatograph Scion 456 (GC) with a pulsed discharge detector and a molecular sieve 5A packed column was used to characterize hydrogen production from the reaction of NP-Al with DI water. A JEOL 7500F scanning electron microscope (SEM)

in combination with energy dispersive X-ray spectroscopy (EDS) were used to characterize the morphology of hierarchical NP-Al and the bulk chemical composition of the corresponding activated alumina. The surface chemical composition of the Al₂O₃ final product was analyzed using X-ray photoelectron spectroscopy (XPS) utilizing a PHI Veraprobe 5000 instrument equipped with a monochromated Al K α radiation source. X-ray diffraction (XRD) patterns were collected on a Rigaku Miniflex powder diffractometer equipped with a Cu X-ray source operated at 40kV/15 mA, theta/2theta goniometer in the Bragg-Brentano parafocusing geometry, Ni foil K-beta filter, and 1D solid state detector. The nanostructured morphology of the Al₂O₃ was also characterized with transmission electron microscopy JEOL 2010F (TEM). Porosity characterization results were conducted using a Micromeritics TriStar II 3020 porosimeter. The adsorption branch of the isotherm was used to calculate the surface area using the Brunauer-Emmett-Teller (BET) model as well as the pore diameter and pore volume using the Barret-Joyner-Halenda (BJH) model.

3. Results and discussion

3.1. Scaling up the synthesis of nanoporous aluminum

Mg stripping from Al-Mg parent alloy and Mg plating onto the Mg foil counter electrode can be considered as a series of electrochemical steps: (1) dissolution of Mg (Mg \rightarrow Mg²⁺ + 2e⁻) at the working electrode; (2) diffusion of Mg^{2+} ions in the electrolyte to the counter electrode, while electrons diffuse through the external circuit; (3) plating of Mg²⁺ ions at the counter electrode $(Mg^{2+} + 2e^{-} \rightarrow Mg)$. This overall electrochemical reaction can be represented by the current measured between the working and counter electrodes arising from the diffusion of electrons through the external circuit. In general, processes affecting mass or electron transfer can affect this current and thus the electrode reaction rate as well. To increase mass transfer, the electrodes are placed within close proximity and the electrolyte resistance to allow for diffusion of Mg²⁺ ions is reduced with the inclusion of LiCl salt in the electrolyte. To increase electron transfer at the electrode surface, the bulk starting alloy was crushed into fine pieces to allow for more surface area and therefore more dissolution sites. Additionally, multiple electrodes can be connected in parallel at the same voltage as mentioned earlier for scalability purposes. Similar concepts in our design are used in commercial copper refining via electrowinning [33]. Fig. 1c and d shows the magnesium counter electrodes used after dealloying. Notice that the Mg is plated on both sides of the middle electrode, showing the beneficial additions of using multiple electrodes for increased counter electrode surface area interactions. The peak current measured was larger in magnitude in comparison to our earlier publication [15], meaning that the reaction rate is occurring much faster with this configuration. Typical SEM images of the created hierarchical NP-Al are shown in Fig. 1e (low magnification) and 1f (high magnification). At low magnification, macropores and macroligaments with characteristic size in the micrometer range are observed (Fig. 1e). At high magnification, ligament/pore structures with characteristic size in the range of 10-20 nm are observed (Fig. 1f). These morphology and structure sizes are in agreement with our previous work [15], meaning that although the present dealloying current magnitude is much larger, the pore size of the produced hierarchical NP-Al was not changed. Using this new configuration, the rate of NP-Al production was ~5 mg per hour. Compared to our previous rate of NP-Al production of ~0.25 mg per hour, this improved configuration shows a twenty-fold increase in production capabilities [15]. Thus, production scalability for mass commercialization can be realized by following these three demonstrated principles.

3.2. Gas chromatography study of H_2 production by hydrolysis of nanoporous aluminum with pure water

The cumulative amount of hydrogen produced as a function of the reaction time from NP-Al and H₂O is shown in Fig. 2. The first ten data points (black square) were fit from experimental values over the course of 24 h. and the rest of the curve (solid red line) was extrapolated for several days. The data matches our previous work. emphasizing the reproducibility of these results. For 3 days of reaction time, the reaction yield is extrapolated to be ~70%, and for 7 days, the reaction yield is ~84%. Although the reaction is not predicted to have reached completion at this point, the reaction was visibly no longer producing hydrogen gas bubbles in solution. This is most likely due to the formation of an Al(OH)₃ envelope preventing further reaction of Al with DI H_2O [34–36]. It is important to note that our process for generating hydrogen gas from NP-Al is not optimized. Varying the ratio of water to aluminum can cause variations to the reaction time length scale as analyzed by Chen et al. [37] Surface area, temperature, pH, particle size effects, ultrasonic agitation, and adding other additives can lead to different hydrogen gas yield reaction rates as well [38-41]. While the rate of reaction can be improved, it is not the objective of this research to find methods of improvement from standard conditions; rather it is to examine the state of the converted products formed from this proposed solution for hydrogen production and storage.

3.3. Co-production of H_2 , $Al(OH)_3$, and heat by hydrolysis of nanoporous aluminum with pure water

The XRD patterns of hierarchical NP-Al before and after its reaction with DI H₂O are presented in Fig. 3. The NP-Al is face-centered cubic (FCC) as shown by the black pattern. The corresponding Al(OH)₃ powder formed after the reaction is shown by the red pattern. This product exhibits a single phase of bayerite Al(OH)₃ distinguished by its first peak at 18.785° as opposed to the gibbsite Al(OH)₃ phase, which has its first peak at 18.392° [37]. The single-phase formation of bayerite observed agrees with other literature results of forming aluminum hydroxide from aluminum and water [26,27]. The formation of Al₂O₃ or other aluminum species such as boehmite AlO(OH) were not observed by XRD from

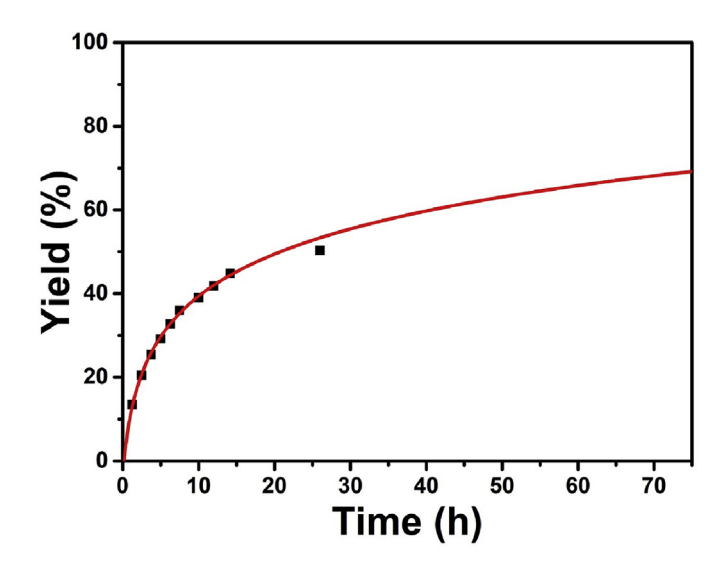


Fig. 2. Black square: GC data associated with hydrogen yield from the reaction of hierarchical nanoporous aluminum with pure water. Red curve: exponential fit extrapolated over 3 days. (For interpretation of the references to color in this figure legend, the reader is referred to the Web version of this article.)

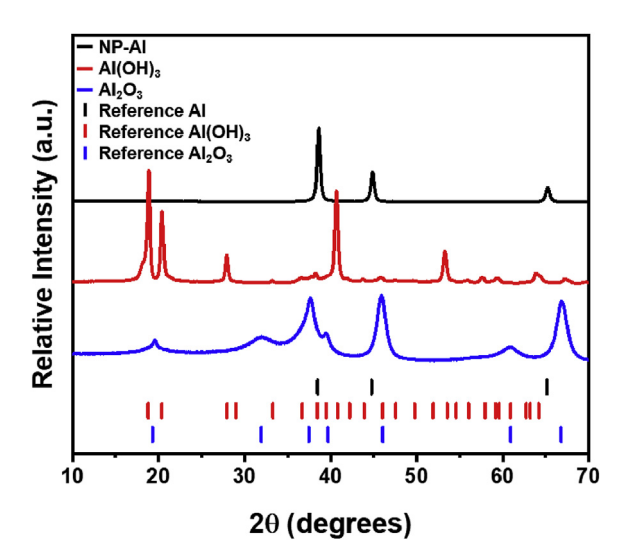


Fig. 3. XRD Patterns for hierarchical NP-Al (black), Al(OH)₃ (red), and Al₂O₃ (blue) with crystallography reference vertical stick patterns for FCC Al (black, PDF #00-004-0787), Bayerite Al(OH)₃ (red, PDF #00-012-0457), and η -Al₂O₃ (blue, PDF #00-004-0875). (For interpretation of the references to color in this figure legend, the reader is referred to the Web version of this article.)

the reaction of NP-Al and Dl H₂O. Analysis of the incomplete product transformation of Al(OH)₃ in Supplementary Fig. S1 shows two phases: the single bayerite Al(OH)₃ product and the original FCC Al. The data indicates an incomplete reaction, which is in agreement with GC results suggesting only a 70% reaction yield after 3 days. This data also suggests that no other phases or Al species are detected during the transformation from Al to Al(OH)₃.

3.4. Conversion of Al(OH)₃ into activated alumina η -Al₂O₃ with high specific surface area

Heat treatment triggers dehydroxylation of the aforementioned Al(OH)₃ powders to form Al₂O₃ samples. The final product, a fine white powder, is shown in Fig. 4b in comparison to the starting black NP-Al pieces in Fig. 4a. The blue pattern in Fig. 3 shows the XRD results corresponding to the final Al₂O₃ product shown in Fig. 4b. The thermal decomposition of bayerite Al(OH)₃ to alumina has been known to transition through different metastable phases, forming η -Al₂O₃ at temperatures between 300 °C and 600 °C, then θ -Al₂O₃ between 600 °C and 1100 °C, and finally the thermodynamically stable phase of α -Al₂O₃ above 1100 °C [27,31]. Thus, we see the single-phase formation of η -Al₂O₃ after heat treatments at

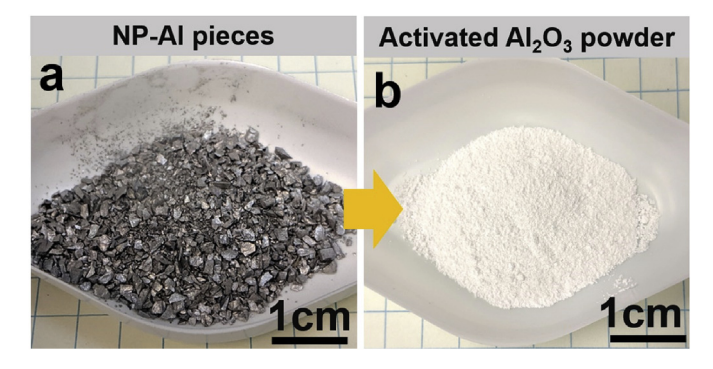


Fig. 4. (a) Hierarchical NP-Al from large-scale production and (b) corresponding activated Al_2O_3 powder obtained from $Al(OH)_3$ co-produced with H_2 by hydrolysis of the NP-Al from (a).

600 °C. The diffraction peaks are reasonably broad regardless of reaction time because of the reduced crystallite size and lattice strain from the thermal decomposition process. Transformation to other phases outside of η -Al₂O₃ are possible using chemical additives; these transformation routes focus on lowering the activation energy for the nucleation of other transition Al₂O₃ phases [42,43]. These processes may be useful for future optimization procedures. Analysis of the XRD patterns for the incomplete transformation product of Al₂O₃ in Fig. S1 exhibits a mixture of alumina and unreacted aluminum. The lack of complete conversion of Al even during the open-air heating process to form Al₂O₃ is consistent with an inner composition of Al, protected by an outer layer of oxidized species [34–36].

EDS data showing the composition of the final Al₂O₃ product are summarized in Table 2. An Al-to-O ratio of ~0.689 is deduced from these EDS data, which is very close to the Al-to-O ratio of 0.667 expected for Al₂O₃. A ~2 at. % residual Mg remains in the sample due to incomplete dealloying. XPS characterization data are shown in Fig. 5. The deconvoluted Al 2p peak in Fig. 5a reveals that ~95.23% of Al is in the form of Al³⁺ from Al₂O₃, detected at 74.5 eV, and some ~4.77% metallic Al detected at 72.7 eV [44,45]. It is expected that some unreacted Al will be detected because the extrapolated reaction yield is only 84% by GC; however, the presence of metallic Al near the surface might be minimized compared to the bulk. The deconvoluted O 1s peak in Fig. 5b suggests that ~94.66% of the nearsurface oxygen atoms are involved in O-Al bonds from Al₂O₃, with peak at 531.3 eV, while ~5.14% of the near-surface oxygen atoms come from adsorbed water molecules, with peak at 534.7 eV [46.47]. No peak associated with Al(OH)₃ was detected at ~532.4 eV. indicating the full conversion from Al(OH)₃ to Al₂O₃ [46]. The presence of adsorbed water molecules near the surface of activated alumina as suggested from XPS data is interesting; indeed, since the samples were activated at 600 °C for 12 h, all near-surface water molecules and hydroxyl groups are removed during this heat treatment step. Consequently water molecules near the surface of activated Al₂O₃ can only come from post adsorption of moisture, when these samples are exposed to air. This good adsorption capability of activated alumina justifies its usage in applications such as water filtration for fluoride treatment, hydrocarbon impurity capture in the automobile and petroleum industries, or as a desiccant for drying gases [23-25].

The typical nanoscale morphology of the activated $\eta\text{-}Al_2O_3$ product as obtained from TEM characterization is shown at different magnifications in Fig. 6. The material exhibits an ultra-fine nanoporous morphology, with ligaments in the range of ~2–5 nm and pores in the range of ~4–6 nm, which are much smaller than the ~10–20 nm ligament/pore structures present in the starting NP-Al before the hydrolysis reaction to produce H_2 and $Al(OH)_3$. As mentioned earlier, the origin of these pores are from the removal of hydroxide groups from the $Al(OH)_3$ precursor in the form of H_2O and not from the nanostructuring created during electrochemical dealloying. This explains why the characteristic pore size in activated alumina (4–6 nm) is much smaller than in NP-Al (10–20 nm). A line scan EDS across a bright field STEM image (not shown) of the activated $\eta\text{-}Al_2O_3$ product reveals that the elements detected are Al, O, and residual Mg in agreement with the EDS results from Table 2.

To further confirm the nanoporous morphology observed from

Table 2Typical EDS data showing the chemical composition of activated Al₂O₃ obtained by heat treatment of the Al(OH)₃ hydrolysis byproduct.

Element	Al	Mg	0
Composition (at. %)	40	2	58

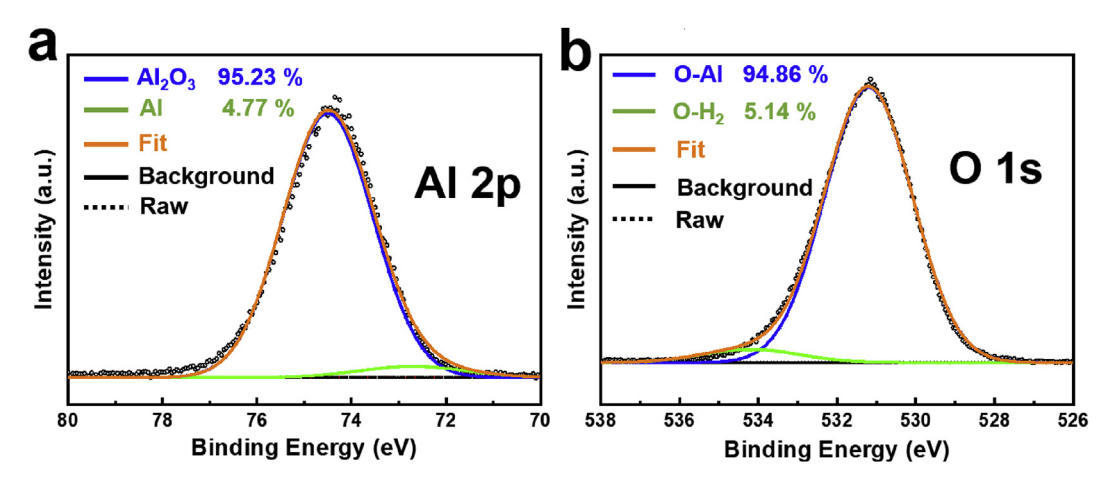


Fig. 5. High resolution XPS spectra of Al 2p (a) and O 1s (b) peaks obtained from activated alumina. In (a) \sim 95.23% of aluminum has been converted into Al₂O₃, with only \sim 4.77% of unreacted residual Al. In (b) \sim 5.14% of near-surface oxygen atoms comes from water molecules post adsorbed in the pores of activated alumina.

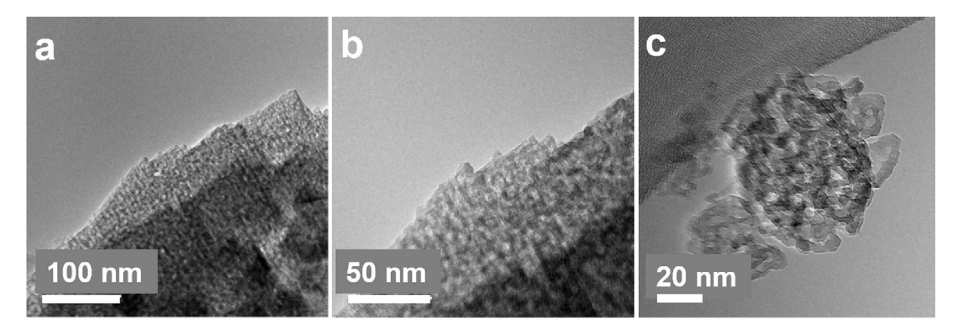


Fig. 6. TEM images of activated Al₂O₃ at different magnifications. A nanoporous morphology with a characteristic pore size around ~4–6 nm is observed at high magnification.

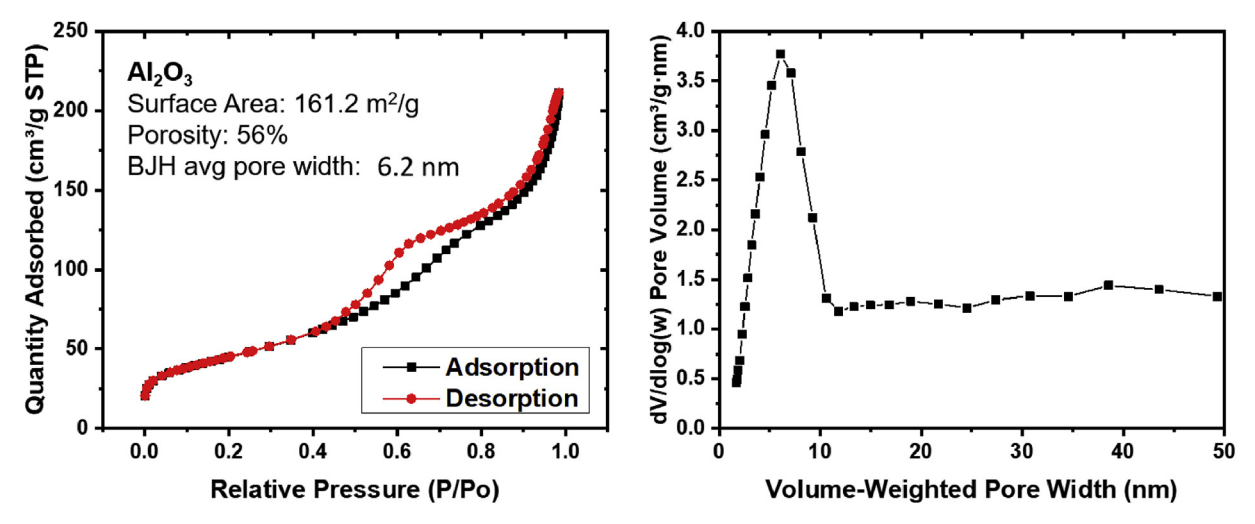


Fig. 7. Adsorption and desorption isotherms (left) and BJH adsorption volume-weighted pore size distribution (right) of activated Al₂O₃.

TEM images (see Fig. 6), nitrogen porosimetry measurements were performed on the activated η -Al₂O₃ product. The adsorption (black) and desorption (red) isotherms are shown in Fig. 7. The isotherm is a combination of a Type IV isotherm (up to P/P₀ = 0.8) typical of mesopores, and a Type III isotherm (from P/P₀ = 0.8–1.0) typical of macropores [48]. Using these curves, the BET method was used to obtain the surface area of the activated Al₂O₃ samples, which was determined to be 161.2 m²/g. The BJH adsorption average pore

width is 6.3 nm, while the BJH adsorption volume-weighted pore size distribution shows a peak at 6.1 nm. The hysteresis in the adsorption and desorption isotherms from 0.4 to 0.8 P/P₀ (Type H1/H2) indicates that the pores have a smaller neck size around ~5.2 nm (BJH desorption), while the hysteresis above 0.8 P/P₀ (Type H3) could be due to the ligament structure [48]. These results are in agreement with the characteristic pore size obtained from TEM. Nitrogen porosimetry measurements performed on the

Table 3Comparison of BET surface area for different activated Al₂O₃ samples.

	Incomplete Al ₂ O ₃	Activated Al ₂ O ₃	Commercial (Alfa)
BET Surface Area (m ² /g)	95.47	161.2	220-260
BJH adsorption average pore width (nm)	7.1	6.2	9
Porosity	39.8%	56.4%	Not Available

"incompletely" converted Al_2O_3 sample (from Fig. S1) indicates that the partially-activated Al_2O_3 exhibits lower porosity, stemming from the lower reaction yield in producing $Al(OH)_3$ from hierarchical NP-Al. While the $161.2~m^2/g$ measured in the fully converted η -Al $_2O_3$ is high, it should be mentioned that this value is relatively lower than the specific surface area of commercial activated γ -Al $_2O_3$ from Alfa Aesar (Catalog no. 43832, catalyst support, high surface area, bimodal), as shown in Table 3. Thus, optimization processes to maximize the specific surface area like those used presumably in industry for commercial activated alumina products are necessary for further improvements to the hydrogen gas production value proposition.

4. Conclusion

In this research, the scalability and value-added byproduct of hydrogen gas production via the hydrolysis reaction of nanoporous aluminum with pure water were investigated. A 20-fold improvement in the dealloying rate to produce nanoporous aluminum was demonstrated using three strategies: increasing the ionic conductivity of the electrolyte, the surface area of the electrodes, and the number of electrodes simultaneously used in the cell. The transformation of NP-Al was also analyzed and shown to produce bayerite Al(OH)₃ after reaction with water. Thermal decomposition of bayerite Al(OH)₃ led to activated η -Al₂O₃ with a high surface area of 161.2 m²/g. The surface area of activated alumina can be affected by various reaction or synthesis conditions producing different metastable phases of Al(OH)₃ or Al₂O₃. Thus, for commercial viability of the activated η -Al₂O₃ product produced by this method, optimization towards even higher surface areas is recommended for future applications of this reaction process.

Declaration of competing interest

There are no conflicts to declare.

CRediT authorship contribution statement

Timothy Lee: Writing - original draft, Data curation. **Jintao Fu:** Writing - review & editing, Data curation. **Victoria Basile:** Writing - review & editing, Data curation. **John S. Corsi:** Writing - review & editing, Data curation. **Zeyu Wang:** Writing - review & editing, Data curation. **Eric Detsi:** Conceptualization, Funding acquisition, Project administration, Resources, Software, Supervision, Validation, Visualization, Writing - review & editing.

Acknowledgements

The authors are thankful to the National Science Foundation (NSF) for their financial support through the NSF-EAGER program with Award number: CMMI-1840672 (E. Detsi) and through the 2019 NSF GRFP with Award Number: DGE-1845298 (T. Lee). The authors are also thankful to the Vagelos Institute for Energy Science and Technology (VIEST) for their support through the VIEST Graduate Fellowship support (J.S. Corsi). Lastly, the authors would like to acknowledge the Singh Center for Nanotechnology, part of the

National Nanotechnology Coordinated Infrastructure Program, which is supported by the National Science Foundation grant NNCI-1542153.

Appendix A. Supplementary data

Supplementary data to this article can be found online at https://doi.org/10.1016/j.renene.2020.03.072.

References

- R. Kothari, D. Buddhi, R.L. Sawhney, Comparison of environmental and economic aspects of various hydrogen production methods, Renew. Sustain. Energy Rev. 12 (2008) 553–563, https://doi.org/10.1016/j.rser.2006.07.012.
- [2] K. Zeng, D. Zhang, Recent progress in alkaline water electrolysis for hydrogen production and applications, Prog. Energy Combust. Sci. 36 (2010) 307–326, https://doi.org/10.1016/j.pecs.2009.11.002.
- [3] P. Nikolaidis, A. Poullikkas, A comparative overview of hydrogen production processes, Renew. Sustain. Energy Rev. 67 (2017) 597–611, https://doi.org/ 10.1016/j.rser.2016.09.044.
- [4] D.C. Upham, V. Agarwal, A. Khechfe, Z.R. Snodgrass, M.J. Gordon, H. Metiu, E.W. McFarland, Catalytic molten metals for the direct conversion of methane to hydrogen and separable carbon, Science 80 (2017), https://doi.org/10.1126/ science.aao5023.
- [5] J. Ashok, P.S. Reddy, G. Raju, M. Subrahmanyam, A. Venugopal, Catalytic decomposition of methane to hydrogen and carbon nanofibers over Ni-Cu-SiO2 catalysts, Energy Fuel. (2009), https://doi.org/10.1021/ef8003976.
- [6] A. Venugopal, S. Naveen Kumar, J. Ashok, D. Hari Prasad, V. Durga Kumari, K.B.S. Prasad, M. Subrahmanyam, Hydrogen production by catalytic decomposition of methane over Ni/SiO2, Int. J. Hydrogen Energy (2007), https:// doi.org/10.1016/j.jihydene.2007.01.007.
- [7] H.F. Abbas, W.M.A. Wan Daud, Hydrogen production by methane decomposition: a review, Int. J. Hydrogen Energy (2010), https://doi.org/10.1016/j.ijhydene.2009.11.036.
- [8] M. Pudukudy, Z. Yaakob, Methane decomposition over Ni, Co and Fe based monometallic catalysts supported on sol gel derived SiO2 microflakes, Chem. Eng. J. (2015), https://doi.org/10.1016/j.cej.2014.10.077.
- [9] M. Pudukudy, Z. Yaakob, Z.S. Akmal, Direct decomposition of methane over SBA-15 supported Ni, Co and Fe based bimetallic catalysts, Appl. Surf. Sci. (2015), https://doi.org/10.1016/j.apsusc.2015.01.032.
- [10] S. Takenaka, S. Kobayashi, H. Ogihara, K. Otsuka, Ni/SiO2catalyst effective for methane decomposition into hydrogen and carbon nanofiber, J. Catal. (2003), https://doi.org/10.1016/S0021-9517(02)00185-9.
- [11] Y. Li, B. Zhang, X. Xie, J. Liu, Y. Xu, W. Shen, Novel Ni catalysts for methane decomposition to hydrogen and carbon nanofibers, J. Catal. (2006), https:// doi.org/10.1016/j.jcat.2005.12.027.
- [12] M.A.A. Aziz, A.A. Jalil, S. Triwahyono, R.R. Mukti, Y.H. Taufiq-Yap, M.R. Sazegar, Highly active Ni-promoted mesostructured silica nanoparticles for CO2 methanation, Appl. Catal. B Environ. (2014), https://doi.org/10.1016/ iancath 2013 09 015
- [13] J.I. Villacampa, C. Royo, E. Romeo, J.A. Montoya, P. Del Angel, A. Monzón, Catalytic decomposition of methane over Ni-Al2O3 coprecipitated catalysts Reaction and regeneration studies, Appl. Catal. Gen. (2003), https://doi.org/ 10.1016/S0926-860X(03)00492-7.
- [14] N. Laosiripojana, W. Sutthisripok, S. Assabumrungrat, Synthesis gas production from dry reforming of methane over CeO2 doped Ni/Al2O3: influence of the doping ceria on the resistance toward carbon formation, Chem. Eng. J. (2005), https://doi.org/10.1016/j.cej.2005.06.003.
- [15] J.S. Corsi, J. Fu, Z. Wang, T. Lee, A.K. Ng, E. Detsi, Hierarchical bulk nanoporous aluminum for on-board generation of hydrogen by hydrolysis in Pure Water and Catalytic Combustion of Solid Fuels, Under Rev. (n.d.).
- [16] S.K. Das, J.A.S. Green, Aluminum industry and climate change-Assessment and responses, JOM (2010), https://doi.org/10.1007/s11837-010-0027-5.
- [17] A. Gupta, B. Basu, Sustainable primary aluminium production: Technology status and future opportunities, Trans. Indian Inst. Met. (2019), https:// doi.org/10.1007/s12666-019-01699-9.
- [18] Global Aluminum Scrap Recycling Market, 2019.
- [19] Department of Energy Office of Energy Efficiency and Renewable Energy Funding Opportunity Announcement Number: DE-FOA-0002022 Table of Contents, 2019.
- [20] M. Trueba, S.P. Trasatti, γ -alumina as a support for catalysts: a review of

- fundamental aspects, Eur. J. Inorg. Chem. (2005), https://doi.org/10.1002/eijc.200500348
- [21] D.T. Lundie, A.R. McInroy, R. Marshall, J.M. Winfield, P. Jones, C.C. Dudman, S.F. Parker, C. Mitchell, D. Lennon, Improved description of the surface acidity of η-alumina, J. Phys. Chem. B (2005), https://doi.org/10.1021/jp0405963.
- [22] K. Sohlberg, S.T. Pantelides, S.J. Pennycook, Surface reconstruction and the difference in surface acidity between γ- and η-alumina, J. Am. Chem. Soc. (2001), https://doi.org/10.1021/ja002095a.
- [23] R. Wischert, P. Laurent, C. Copéret, F. Delbecq, P. Sautet, γ-Alumina: the essential and unexpected role of water for the structure, stability, and reactivity of "defect" sites, J. Am. Chem. Soc. (2012), https://doi.org/10.1021/ ja3042383.
- [24] W. Cai, J. Yu, M. Jaroniec, Template-free synthesis of hierarchical spindle-like γ-Al 2O3 materials and their adsorption affinity towards organic and inorganic pollutants in water, J. Mater. Chem. (2010), https://doi.org/10.1039/ b02/366f
- [25] A. Srivastav, V.C. Srivastava, Adsorptive desulfurization by activated alumina, J. Hazard Mater. (2009), https://doi.org/10.1016/j.jhazmat.2009.05.088.
- [26] A. Savel'eva, T. Bugrova, A. Petrov, V. Dutov, G. Mamontov, Thermally-activated Al(OH)₃: phase transformations and porosity, Key Eng. Mater. (2015). https://doi.org/10.4028/www.scientific.net/kem.670.133.
- [27] A.S. Ivanova, Aluminum oxide and systems based on it: properties and applications, Kinet. Catal. (2012), https://doi.org/10.1134/s0023158412040039.
- [28] H. Yaghoobnejad Asl, J. Fu, H. Kumar, S.S. Welborn, V.B. Shenoy, E. Detsi, In situ dealloying of bulk Mg2Sn in Mg-ion half cell as an effective route to nanostructured Sn for high performance Mg-ion battery anodes, Chem. Mater. (2018), https://doi.org/10.1021/acs.chemmater.7b04124.
- [29] Z. Wang, A. Bandyopadhyay, H. Kumar, M. Li, A. Venkatakrishnan, V.B. Shenoy, E. Detsi, Degradation of magnesium-ion battery anodes by galvanic replacement reaction in all-phenyl complex electrolyte, J. Energy Storage (2019), https://doi.org/10.1016/j.est.2019.02.022.
- [30] J. Bitenc, M. Firm, A. Randon Vitanova, R. Dominko, Effect of Cl—and TFSI—anions on dual electrolyte systems in a hybrid Mg/Li4Ti5O12battery, Electrochem. Commun. (2017), https://doi.org/10.1016/j.elecom.2017.01.013.
- [31] A. Pearson, Aluminum oxide (alumina), activated, in: Kirk-Othmer Encycl. Chem. Technol., 2004, https://doi.org/10.1002/ 0471238961.0103200916050118.a01.
- [32] X. Du, Y. Wang, X. Su, J. Li, Influences of pH value on the microstructure and phase transformation of aluminum hydroxide, Powder Technol. (2009), https://doi.org/10.1016/j.powtec.2008.11.008.
- [33] F. Cuevas, C. Murray, W. Platzer, A. Heimsath, Large scale solar plants integration in electro-winning copper recuperation process, Energy Procedia (2015), https://doi.org/10.1016/j.egypro.2015.02.167.
- [34] US DOE, Reaction of Aluminum with Water to Produce Hydrogen, 2008.
- [35] L. Soler, A.M. Candela, J. Macanás, M. Muñoz, J. Casado, Hydrogen generation by aluminum corrosion in seawater promoted by suspensions of aluminum hydroxide, Int. J. Hydrogen Energy 34 (2009) 8511–8518, https://doi.org/ 10.1016/j.ijhydene.2009.08.008.

- [36] H. Te Teng, T.Y. Lee, Y.K. Chen, H.W. Wang, G. Cao, Effect of Al(OH) 3 on the hydrogen generation of aluminum-water system, J. Power Sources (2012), https://doi.org/10.1016/j.jpowsour.2012.06.077.
- [37] Y.K. Chen, H. Te Teng, T.Y. Lee, H.W. Wang, Rapid hydrogen generation from aluminum-water system by adjusting water ratio to various aluminum/ aluminum hydroxide, Int. J. Energy Environ. Eng. 5 (2014) 1–6, https:// doi.org/10.1007/s40095-014-0087-3.
- [38] Y. Yavor, S. Goroshin, J.M. Bergthorson, D.L. Frost, R. Stowe, S. Ringuette, Enhanced hydrogen generation from aluminum-water reactions, Int. J. Hydrogen Energy 38 (2013) 14992–15002, https://doi.org/10.1016/ i.iihvdene.2013.09.070.
- [39] S.O. Kazantsev, A.S. Lozhkomoev, E.A. Glazkova, I. Gotman, E.Y. Gutmanas, M.I. Lerner, S.G. Psakhie, Preparation of aluminum hydroxide and oxide nanostructures with controllable morphology by wet oxidation of AlN/Al nanoparticles, Mater. Res. Bull. (2018), https://doi.org/10.1016/ i.materresbull.2018.04.011.
- [40] A.I. Osman, J.K. Abu-Dahrieh, D.W. Rooney, S.A. Halawy, M.A. Mohamed, A. Abdelkader, Effect of precursor on the performance of alumina for the dehydration of methanol to dimethyl ether, Appl. Catal. B Environ. (2012), https://doi.org/10.1016/j.apcatb.2012.08.033.
- [41] E.V. Kul'ko, A.S. Ivanova, V.Y. Kruglyakov, E.M. Moroz, K.I. Shefer, G.S. Litvak, G.N. Kryukova, Y.Y. Tanashev, V.N. Parmon, Synthesis of aluminum oxides from the products of the rapid thermal decomposition of hydrargillite in a centrifugal flash reactor: II. Structural and textural properties of aluminum hydroxide and oxide obtained from the product of the centrifugal thermal, Kinet. Catal. (2007), https://doi.org/10.1134/s0023158407020176.
- [42] X. Du, X. Su, Y. Wang, J. Li, Thermal decomposition of grinding activated bayerite, Mater. Res. Bull. (2009), https://doi.org/10.1016/ j.materresbull.2008.06.031.
- [43] Z.Y. Deng, Y.F. Liu, Y. Tanaka, J. Ye, Y. Sakka, Modification of AI particle surfaces by γ-Al 2O 3 and its effect on the corrosion behavior of AI, J. Am. Ceram. Soc. (2005), https://doi.org/10.1111/j.1551-2916.2005.00154.x.
- [44] M. Liu, S. Zanna, H. Ardelean, I. Frateur, P. Schmutz, G. Song, A. Atrens, P. Marcus, A first quantitative XPS study of the surface films formed, by exposure to water, on Mg and on the Mg-Al intermetallics: Al3Mg2 and Mg17Al12, Corrosion Sci. (2009), https://doi.org/10.1016/j.corsci.2009.02.017.
- [45] J.T. Kloprogge, L.V. Duong, B.J. Wood, R.L. Frost, XPS study of the major minerals in bauxite: gibbsite, bayerite and (pseudo-)boehmite, J. Colloid Interface Sci. (2006), https://doi.org/10.1016/j.jcis.2005.09.054.
- [46] N. Kumar, K. Biswas, Cryomilling: an environment friendly approach of preparation large quantity ultra refined pure aluminium nanoparticles, J. Mater. Res. Technol. (2019), https://doi.org/10.1016/j.jmrt.2017.05.017.
- [47] A. Ganguly, S. Sharma, P. Papakonstantinou, J. Hamilton, Probing the thermal deoxygenation of graphene oxide using high-resolution in situ X-ray-based spectroscopies, J. Phys. Chem. C (2011), https://doi.org/10.1021/jp203741y.
- [48] M. Thommes, K. Kaneko, A.V. Neimark, J.P. Olivier, F. Rodriguez-Reinoso, J. Rouquerol, K.S.W. Sing, Physisorption of gases, with special reference to the evaluation of surface area and pore size distribution, IUPAC Technical Report, Pure Appl. Chem. (2015), https://doi.org/10.1515/pac-2014-1117.